HHS Public Access

Author manuscript

IEEE Trans Biomed Eng. Author manuscript; available in PMC 2023 August 01.

Published in final edited form as:

IEEE Trans Biomed Eng. 2022 August ; 69(8): 2679–2690. doi:10.1109/TBME.2022.3152212.

Experimental Study of Aperiodic Plane Wave Imaging for Ultrafast 3-D Ultrasound Imaging

Sua Bae,
University, Seoul, Republic of Korea.

Bae-Hyung Kim [Senior Member, IEEE],
Mayo Clinic College of Medicine and Science, Rochester, MN, USA.

Azra Alizad [Senior Member, IEEE],
Mayo Clinic College of Medicine and Science, Rochester, MN, USA.

Mostafa Fatemi [Life Fellow, IEEE],
Mayo Clinic College of Medicine and Science, Rochester, MN, USA.

Tai-Kyong Song [Member, IEEE]
Sogang University, Seoul, Republic of Korea.

Abstract

Objective: Although plane wave imaging (PWI) with multiple plane waves (PWs) steered at different angles enables ultrafast three-dimensional (3-D) ultrasonic imaging, there is still a challenging tradeoff between image quality and frame rate. To address this challenge, we recently proposed the aperiodic PWI (APWI) with mathematical analysis and simulation study. In this paper, we demonstrate the feasibility of APWI and evaluate the performance with phantom and *in vivo* experiments.

Methods: APWI with a concentric ring angle pattern (APWI-C) and APWI with a sunflower pattern (APWI-S) are evaluated. For experimental verification of the methods, the experimental results are compared with simulation results in terms of the spatial resolution and the mainlobe-to-sidelobe ratio. In addition, the performance of APWI is compared with that of conventional PWI by using a commercial phantom. To examine the potential for clinical use of APWI, a gallstone-mimicking phantom study and an *in vivo* carotid artery experiment are also conducted.

Results: In the phantom study, the APWI methods provide a contrast ratio approximately 2–3 dB higher than that of PWI. In a gallstone mimicking experiment, the proposed methods yield 3-D rendered stone images more similar to the real stones than PWI. In the *in vivo* carotid artery images, APWI reduces the clutter artifacts inside the artery.

Conclusion: Phantom and *in vivo* studies show that the APWI enhances the contrast without compromising the spatial resolution and frame rate.

Significance: This study experimentally demonstrates the feasibility and advantage of APWI for ultrafast 3-D ultrasonic imaging.

correspondence tksong@sogang.ac.kr, fatemi.mostafa@mayo.edu, alizad.azra@mayo.edu.

Keywords

3-D ultrasonic imaging; aperiodic plane wave angle pattern; coherent plane wave compounding; contrast enhancement; ultrafast ultrasound imaging

I. Introduction

Three-dimensional (3-D) ultrasound (US) imaging has been shown to provide numerous advantages relative to traditional two-dimensional (2-D) US imaging in various clinical applications with respect to diagnostic accuracy and efficiency [1], [2]. The quality of 3-D US imaging is determined mainly by the spatial resolution and contrast resolution. In addition, the scanning rate per volume is also important to obtain a volumetric image with less motion artifact.

In traditional 3-D US with a one-dimensional (1-D) array transducer, the spatial resolution perpendicular to the array (i.e., in the elevational direction) is much worse than that parallel to the array (i.e., in the lateral direction) because fixed focusing is used in the former, while dynamic focusing is achieved in the latter. However, with the development of 2-D matrix array transducers, it became possible to dynamically focus a beam in both the lateral and elevational directions [3].

Real-time scanning is a key advantage of 3-D US imaging over other medical imaging modalities. Multiplane imaging, in which two or three orthogonal cross-sectional images are acquired and displayed in real time, is commercialized and being used in clinic. However, a full 3-D volume scanning is challenging to achieve at a real-time frame rate with the traditional focusing technique, where a focused beam is transmitted along each scanline to acquire a volume comprising tens of thousands of scanlines. To maintain the real-time imaging ability of 3-D US, new scanning techniques have been developed, such as the multiline acquisition [4]–[8] or multiline transmission (TX) technique [9]–[12] and synthetic focusing techniques [13], [14].

In addition to the focused beam, unfocused beams such as plane waves (PWs) or diverging waves are also used to synthetically form a sharp ultrasonic beam for higher frame rates [2], [15]–[19]. These synthetic focusing techniques with unfocused beams have been applied to various 3-D imaging applications, including blood flow imaging [20]–[22], tissue elasticity imaging [23]–[25], and cardiac fiber orientation imaging [26]. In PW imaging (PWI), also known as coherent PW compounding or PW synthetic focusing, PWs with different steering angles are transmitted by a matrix array transducer and coherently compounded for synthetic transmit focusing.

In PWI, the PW angles need to be carefully selected because the distribution of angles is closely associated with the image quality. The PW angles (or directions) in both 2-D and 3-D PWI are generally distributed periodically with a constant interval [2], [16], [27]–[29]. However, the periodicity of PW angles with a regular interval is known to cause grating lobe artifacts in 2-D PWI with a one-dimensional (1-D) array transducer [27], [28], [30]. By decreasing the interval, these grating lobes can be shifted away from the main lobe,

thereby diminishing the artifacts and enhancing the contrast of the image. However, to do so, either the number of PWs must be increased or the total range of angles must be decreased, compromising either the frame rate or the spatial resolution, respectively, because the number of PWs determines the frame rate and the PW angle range regulates the synthetic beam width.

Recently, we showed that the same association between the angle distribution and image quality was also observed in 3-D PWI with a matrix array transducer [31]. In the study, we proposed aperiodic PWI (APWI), in which an aperiodic angle pattern is used to avoid the periodicity of angles and to enhance the image contrast without compromising the frame rate or spatial resolution. The propagation direction (steering angle) of a PW transmitted by a matrix array transducer (as shown in Fig. 1) is defined by two variables, namely, the lateral (θ) and elevational (ϕ) angles [15]. Therefore, the PW angles used for 3-D PWI can be plotted on a 2-D space representing the lateral and elevational angles. In the previous study, we proposed APWI methods using two types of aperiodic angle distributions: (concentric ring pattern and sunflower pattern) to avoid the periodicity of angles while maintaining a uniform density [31]. We showed that both APWI with a concentric ring angle pattern (APWI-C) and APWI with a sunflower angle pattern (APWI-S) reduce grating lobe artifacts and enhance the contrast and frame rate of 3-D US imaging. However, our previous study presented only theoretical analyses and simulation results.

In this study, we first verified the theoretical (simulation) analyses by experiments with wires in a water tank. We also evaluated the APWI methods compared to the traditional PWI by a commercial quality-assurance phantom. To demonstrate the feasibility and examine the potential for clinical use of APWI, an experiment using a gallbladder-mimicking phantom and an *in vivo* carotid artery experiment were conducted. In addition, we suggested a modified version of the concentric ring PW angle pattern to control the spatial resolution more precisely for a fairer performance comparison across the imaging methods.

II. Methods

A. Definition of PW Angles

Fig. 1 illustrates the propagation of a PW fired from a matrix array transducer located on the xy plane. Letting θ and ϕ signify the lateral and elevational angles of the PW, respectively, the normal vector of the plane wavefront representing the propagation direction of the PW is denoted as $\overrightarrow{n} = (\alpha, \beta, \gamma)$, where $\alpha = \sin\theta$ and $\beta = \cos\theta \sin\phi$. Note that the angle of a PW can be express by only (α, β) since $\gamma = \sqrt{1 - \alpha^2 - \beta^2}$. Accordingly, we express the angles of the PWs used for 3-D US imaging with (α,β) throughout this paper.

1) Traditional PWI with a Periodic PW Angle Set—In 3-D PWI, the angles or directions of PWs emitted from a matrix array transducer are generally distributed periodically [2], [16], [32]. A periodic PW angle set $\mathbb{T}_p$ can be defined as

$$\mathbb{T}_p = \left\{ (\alpha_n, \beta_n) \middle| \alpha_n = k \cdot \Delta\alpha, \beta_n = l \cdot \Delta\beta, \alpha_n^2 + \beta_n^2 \leq r_0^2 \right\}, \quad (1)$$

where k and l are integers, $\Delta\alpha$ is a regular interval on the α-axis and $\Delta\beta$ is a regular interval on the β-axis. The $\mathbb{T}_p$ is illustrated in Fig. 2(a). Each seed (indicated by a black dot) represents a PW angle. r_0 is the radial range of PW angles in the $\alpha\beta$-plane, which determines the mainlobe width of the beam pattern and thus the spatial resolution of the 3-D US image. In this paper, we used the same interval for α and β ($\Delta\alpha = \Delta\beta$), and the interval was calculated by dividing r_0 by an integer number.

Although most practitioners use PW angles periodically distributed in the angle domain (for example, in the $\theta\varphi$-plane), not in the $\alpha\beta$-plane, we distributed PW angles periodically in the $\alpha\beta$-plane for the sake of analysis and consistency with our previous study. Note that the angle difference between two distributions is negligible and there is no significant performance difference between them, which is discussed in the supporting document.

2) APWI with a Concentric Ring PW Angle Pattern—As the periodicity of PW angles results in grating lobes in the beam pattern of synthesized PWs, ultimately degrading the contrast resolution, we proposed an aperiodic pattern for the distribution of PW angles [31]. To maintain a uniform PW angle density, we suggested two types of aperiodic patterns, a concentric ring pattern and a sunflower pattern, as shown in Fig. 2(b) and Fig. 2(c), respectively.

In the concentric ring pattern (Fig. 2(b)), uniformity is achieved by placing the seeds (each representing a single PW angle) with a constant arc-length interval along concentric rings that have regularly increasing radii. To avoid periodicity, the first seed on each ring has a different angle with respect to the α-axis. The aperiodic PW angle set with the concentric ring pattern $\mathbb{T}_p$ for APWI-C is defined as

$$\begin{aligned}\mathbb{T}_c = \{(\alpha_n, \beta_n) | \alpha_n &= \Delta r \cdot p \cdot \cos(\theta_0[p] + \Delta\theta[p] \cdot q),\\ \beta_n &= \Delta r \cdot p \cdot \sin(\theta_0[p] + \Delta\theta[p] \cdot q),\\ n &= 1, 2, \cdots, N\},\end{aligned} \tag{2}$$

where p =0, 1, …, $P-1$, q = 0, 1, …, $Q[p] - 1$. $P-1$ is the number of concentric rings, and $Q[p]$ is the number of seeds (i.e., PWs) on the p-th ring. $Q[0]$ is the number of seeds at the origin, which means that $Q[0] = 1$, and the sum of all $Q[p]$ (p = 0, 1, …, $P-1$) equals the total number of PWs, N. Δr is the constant radial interval between concentric rings, $\theta_0[p]$ is the angle of the first seed on the p-th ring with respect to the α-axis, and $\Delta\theta[p]$ is the angular interval between the seeds on the p-th ring. All the parameters associated with (2) were calculated as in Appendix B in [31] except for Δr In our previous study, the radius interval, Δr, was $r_0/(P-1)$; hence, the radius of the largest ring equals r_0 The previous version of concentric ring pattern has more seeds on the circle with a radius of r_0 than other patterns do, resulting in a larger effective angular range. Because the effective angular aperture determines the mainlobe beam width and spatial resolution, the spatial resolution of the concentric ring pattern was different than that of other patterns [31]. In this study, we used $\Delta r = r_0/(P - 0.5)$ to achieve a margin of $\Delta r/2$ so that the concentric ring pattern has the same effective angular range (i.e., spatial resolution) as periodic and sunflower patterns. Calculation of all parameters for obtaining this modified concentric ring pattern is

summarized in the supporting document. By using this modified version of the concentric ring pattern, we could control the spatial resolution of APWI more precisely.

3) APWI with a Sunflower PW Angle Pattern—The sunflower pattern is obtained from a Fermat spiral with the golden angle, which has been known as an efficient pattern from nature and has been used for antenna or transducer designs [33]–[35]. We used this unique pattern for the PW angle distribution. The aperiodic PW angle set with the sunflower pattern $\mathbb{T}_s$ for APWI-S is defined as

$$\begin{aligned}\mathbb{T}_s = \{(\alpha_n, \beta_n) | \alpha_n &= r_0\sqrt{n/(N-1)}\cos(n\theta_G),\\ \beta_n &= r_0\sqrt{n/(N-1)}\sin(n\theta_G),\\ n &= 0, 1, \cdots, N-1\},\end{aligned} \tag{3}$$

where the golden angle θ_G is $\pi(\sqrt{5}-1)$. Fig. 2(c) presents an example of a sunflower pattern where no seeds have the same angular position. As in the concentric ring pattern, the PW angles are not aligned in any direction but have a uniform density.

B. Experimental Setup

Phantom and *in vivo* experiments were conducted to verify that the proposed ultrafast APWI enhances the image contrast without degrading the spatial resolution or frame rate. A matrix array transducer (8 MHz, 32×32 elements, Vermon, France) and a US system (Vantage 256, Verasonics Inc., Redmond, WA) were used. To acquire the US data of the full-channel TX and reception (RX) with a 256-channel system, the 1024 elements were divided into four subarrays (256 elements per group), and each of four subarrays was used for TX or RX for all combinations (4×4=16) as in [36]. The 16 acquired echoes were combined to synthesize the full-channel TX/RX data. The transmit delay sampling rate (i.e., system clock speed) of the US system was high enough for precise control of PW angles (see supporting document). Parameters used in experiments were listed in Table I. Since the footprint of the transducer is only 10 mm×10 mm, we obtained a pyramidal-shaped volume with a view angle of 15°. The outermost scanline can be reconstructed by using PWs steered by more than 15° because the minimum angle of PWs that reach out to the outermost scanline is 15°. Thus, the maximum PW steering angle was set to 25° (i.e., r_0 = sin(25°) in Fig. 2) to compound the PWs with a range of at least 10°.

C. Materials and Evaluation Methods

1) Experimental Verification of Simulation Study—We conducted a water-wire phantom experiment to demonstrate our previous simulation study [31]. In the experiment, four nylon wires (diameter = 0.3 mm) were placed parallel to the x axis at depths (z) of 10, 20, 30, and 40 mm in a water tank. In the simulation, a series of point targets along a line with an interval of 1/8 wavelength were used to mimic a wire. The diameter of the wire was not simulated. Four virtual wires were placed at the same locations as the four real wires shown in the 3-D images obtained by the experiment. In both experimental and simulation studies, PWI with a periodic angle pattern, APWI-C, and APWI-S were performed. The number of PWs (N) was 113. We observed the lateral profiles and mainlobe-to-sidelobe energy ratios (MSRs) of real wires and virtual wires in the images obtained from

experimental and simulation studies, respectively, to check if the image quality enhancement of the APWI observed in the simulation study could also be found in the experimental study. The MSR was measured [19] by using

$$MSR = 20\log_{10}(m_{\text{main}}/\mu_{\text{side}}) \tag{4}$$

where m_{main} is the maximum value of the beamformed image within a mainlobe region and the μ_{side} is the mean value of the beamformed image within the sidelobe regions. The m_{main} and μ_{side} were calculated from the 3-D beamformed images after envelope detection and before log compression. The mainlobe and sidelobe regions were selected for each wire, as shown in Fig. S1. The mainlobe region enclosed each wire target, and the sidelobe regions included artifacts that appeared on both sides of the wire to evaluate the level of the grating lobes and sidelobes of the synthetic US beam.

2) Quality-Assurance Phantom—A commercial quality-assurance phantom (040GSE, CIRS Inc., Norfolk, VA) was used to evaluate the spatial and contrast resolution enhancements of the APWI compared with the PWI. The wire targets and cylindrical cysts in the phantom were used to evaluate the spatial and contrast resolutions, respectively. The spatial resolution was evaluated by measuring the full width at half maximum of the wire target, and the contrast ratio (CR) and contrast-to-noise ratio (CNR) were measured by [37] by using

$$\text{CR} = \mu_{\text{b}} - \mu_{\text{c}} \tag{5}$$

$$\text{CNR} = \frac{|\mu_{\text{b}} - \mu_{\text{c}}|}{\sqrt{\sigma_{\text{b}}^2 + \sigma_{\text{c}}^2}} \tag{6}$$

where μ_{b} and μ_{c} are the mean intensities of the background speckle and cyst regions and σ_{b} and σ_{c} are the standard deviations of intensities of the background speckle and cyst regions, respectively. The mean and standard deviation of intensities were measured after log compression without clipping the data. A cylindrical cyst region with a length of 10 mm was chosen, and a 10×10×10 mm^3 cubic region except the cyst region was selected for the background. The contrast measurement area is shown in a supplementary video (MM1).

3) Gallbladder-Mimicking Phantom—To demonstrate the effectiveness of APWI in artifact reduction, the gallbladder-mimicking phantom was fabricated by placing a water-filled balloon with a kidney stone inside a gelatin phantom made of 300-bloom gelatin and cellulose scatterers, as shown in Fig. 3. Since kidney stones appear similar to gallstones in US imaging, we used human kidney stones to substitute for gallstones because of the difficulty in procuring gallstones. One human kidney stone was contained in each balloon (stones A and B), and each balloon was imaged. The 3-D US images were used for rendering 3-D shaded surface images, and the rendering process will be described in section II.D.

4) In Vivo Carotid Artery—To prove the clinical feasibility of APWI, 3-D US images of the right carotid artery of a volunteer were obtained by using periodic, concentric, and sunflower PW sets. The data were acquired by a nonexpert following the scan protocol in [38] and a clinical protocol was exempt as a part of an educational student project under the institutional review board.

The number of PWs (N) was 49 for each imaging method. Three imaging sequences were consecutively performed during diastole to obtain the *in vivo* artery image. The arterial pulsation was monitored in real time with image acquisition starting after the beginning of diastole manually. The acquisition time was 117.6 msec (= 50 μsec × 16 TX/RX × 49 angles × 3 sequences), which was short enough to fall into a relaxation period of the artery. Detailed acquisition setup was described in supporting document.

The contrast of the image was measured to evaluate the clutter artifacts inside the carotid artery by using (5). The volumetric tissue and vessel cavity regions were selected for the bright region (μ_b in (5)) and the dark region (μ_c in (5)). A supplementary video of the contrast measurement region is available (MM3). The homogeneous tissue region is shaded in green, and the carotid artery region is shaded in yellow in MM3. The volumetric region was chosen from $y = -5$ mm to $y = 5$ mm.

D. 3-D Image Reconstruction

N PWs in a PW angle set $\mathbb{T}$($\mathbb{T}_p$, $\mathbb{T}_c$ or $\mathbb{T}_s$ in (1), (2) and (3), respectively) were fired consecutively, and the backscattered echoes were received with a matrix array transducer. Then, a synthesized volume image was reconstructed from the N echo data sets by performing 3-D PW synthetic focusing [31]. In this method, each imaging point is reconstructed by using the only data sets of PWs that propagate through the imaging point as follows:

$$b(\mathbf{x}_f) = w_s \Sigma_{(\alpha_n, \beta_n) \in \mathbb{S}(\mathbf{x}_f)} \Sigma_{m=0}^{M-1} w_{rx} \cdot r_{n,m}(\tau^{n,m}) \cdot e^{-j\omega_0 \tau^{n,m}}, \quad (7)$$

where $r_{n,m}$ is the complex baseband signal of the n-th PW received by the m-th channel and $\tau^{n,m}$ is the beamforming delay. The PW subset $\mathbb{S}(\mathbf{x}_f)$($\mathbb{S}(\mathbf{x}_f) \subset \mathbb{T}$) includes the PWs that pass through the imaging point $\mathbf{x}_f$ while maintaining a planewave front. The region where the planewave front is maintained was geometrically calculated according to the angle of PW and the size of aperture. w_{rx} is the receive apodization window, and w_s is the weighting factor, which is inversely proportional to the number of PWs in the subset $\mathbb{S}(\mathbf{x}_f)$. A Tukey window with a 25% role was used for the receive apodization. The beamformed data $b(\mathbf{x}_f)$ are then log-compressed to form the final 3-D B-mode image.

The 3-D shaded surface image of the gallbladder-mimicking phantom was rendered by using the “surf” function in MATLAB. The height data for an input of the surf function were obtained by detecting the surface of the stone or the bottom of the balloon on every scanline (every grid line parallel to the z axis) with a threshold. From the ceiling of the balloon, the first pixel value greater than the threshold was detected for each scanline, and the axial position (z) of the detected first pixel determined the height of the corresponding

scanline. If no pixels along a scanline were greater than the threshold, the threshold was decreased by 1 dB, and the height-detection process was repeated until it found pixels greater than the updated threshold. The initial threshold in the height-detection process for 3-D surface rendering was carefully selected to obtain the best images in terms of the size and shape of the stones and was applied the same across all three methods (PWI, APWI-S and APWI-C). The US volume data filtered with a median filter ($1\times1\times1$ mm^3) were used for height detection.

III. Results

A. Experimental Verification of Simulation Study

To experimentally demonstrate the image quality enhancement of APWI as verified by simulation in a previous study [31], four wires in a water tank were imaged by using periodic (PWI) and aperiodic angles (APWI-C and APWI-S). Fig. 4(a)–(c) shows 3-D US images of wires obtained from the experiment, and Fig. 4(d)–(f) shows the simulation results using four numerical wires at the same location as those in Fig. 4(a)–(c). Cross-sectional images are provided in Fig. S2 in the supporting document. The wires are shown as a yellow lead parallel to the x axis because hyperechoic pixels correspond to yellow in the color map. Grating lobe/sidelobe artifacts around the wires are shown in blue, which ranges from approximately −23 to −38 dB. As depth increased, the artifacts became stronger, and the spatial resolution was compromised (i.e., the width of wire on the y-axis increased). In the experimental results, the APWI methods (Fig. 4(b) and 4(c)) provide less artifact than the PWI (Fig. 4(a)). Similar results were obtained through the simulation; the APWI-C and APWI-S (Fig. 4(e) and 4(f)) showed reduced artifacts than the PWI (Fig. 4(d)). At the depth of 10 mm (top panels of Fig. 4(a)–(f)), the axial artifact below the wire, which is a typical PWI near field artifact [39], is shown. The axial artifact was also mitigated by APWI methods in both experimental and simulation results.

For each wire, a profile along the y axis was taken from the 3-D beamformed image at $x = 0$ mm, normalized by its maximum value, and plotted on a log scale. Fig. 5 shows the profiles of wires at four depths in the experiment and simulation. In both experimental (Fig. 5(a)–(d)) and simulation (Fig. 5(e)–(h)) results, the sidelobe levels of the APWI-C and APWI-S were lower than those of PWI. Meanwhile, the spatial resolutions (i.e., the mainlobe width of the profile) of the three methods were almost the same. The difference in the full-width-half-maximum of the mainlobe (i.e., −6 dB resolution) between the experiment and the simulation was 0.04 mm in average, which showed the similarity between the experiment and simulation setup.

The profiles in Fig. 5. were not symmetric because the wires are not exactly at $y = 0$ in both simulation and experiment. In the experiment, the wires in the water tank were slightly off from $y = 0$ mm and each point target in the simulation was placed at the same y locations as in the experiment.

Fig. 6 presents the MSRs of the experimental and simulated wire images (Fig. 4) measured by using (4) with selected areas shown in Fig. S1 for the quantitative analysis. At all depths, APWI-C and APWI-S showed higher MSRs than PWI in both the experimental and

simulation results. In addition, the trend of the MSR enhancement (i.e., MSR difference between PWI and APWI) along the depth in the experiment was quite similar to that in the simulation. For example, in both the experimental and simulation results, the MSR enhancement of the APWI methods compared to PWI is higher at a depth of 10 mm than at 30 mm. In addition, at a depth of 40 mm, the MSR of APWI-S is higher than that of APWI-C in both the experiment and simulation.

B. Quality-Assurance Phantom

Fig. 7 shows cross-sections of the 3-D US images of the cylindrical cyst of the commercial quality-assurance phantom reconstructed by using the periodic, concentric ring, and sunflower PW sets (N=81) with a dynamic range of 50 dB. A movie is available showing all the cross-Hs of the 3-D images (MM1). The artifacts inside the cylindrical cyst are stronger in the images of the periodic set (PWI) than in those of the concentric ring and sunflower sets (APWI-C and APWI-S).

Table II lists the CR and CNR measured from the same cylindrical cyst using N = 81, 113, and 149, and the volumetric region defined for contrast measurement is shown in another multimedia file (MM2). The contrast increases with the number of PWs used (N) because the clutter inside the cyst, caused by sidelobes and grating lobes of the beam pattern, decreases with increasing N. Note that the proposed concentric and sunflower angle sets (APWI-C and APWI-S) provide a CR approximately 2–3 dB higher than the periodic set (PWI) for all N.

Fig. 8 shows the wire target images obtained from the commercial phantom by using the periodic and two aperiodic sets (N=81). As seen in Fig. 8(a), the three PW angle sets provide wire images of similar spatial resolution on the xz, yz, and xy planes. The lateral profile in Fig. 8(b) shows similar spatial resolutions among the three methods. Table III lists the measured spatial resolutions of 3 wire targets, which are indicated by the white arrows in the top-left panel of Fig. 8(a). The lateral resolutions were obtained from the 3-D images in Fig. 8(a), while the elevational resolutions were measured from another 3-D image acquired by rotating the transducer so that the wires in the phantom were aligned along the x axis of the transducer. Table III also demonstrates that all the methods have similar lateral and elevational resolutions. The results shown in Fig. 8 and Table III are consistent with the theoretical analysis in [31]; that is, the spatial resolution remains the same regardless of the angle distribution pattern when the same range of PW angles (i.e., r_0 in Fig. 2) is used.

C. Gallbladder-Mimicking Phantom

Fig. 9 presents cross-sections of the 3-D US images of the gallbladder-mimicking phantom (stones A and B) reconstructed by PWI, APWI-C, and APWI-S (N=81). The hyperechoic stone lying inside the balloon is shown on the xz- and yz-planes. The top view (xy plane) reveals the balloon wall surrounding the stone. As the white arrows and the yellow boxes in Fig. 9 indicate, the artifacts around the stones were reduced by approximately 3–10 dB in the APWI-C and APWI-S images compared to the PWI image.

Fig. 10(a) presents photos of stones A and B used for the gallbladder-mimicking phantom, and Fig. 10(b) shows top views of the 3-D surface images rendered by using the 3-D US

images in Fig. 9. Whereas the APWI methods reconstructed the shapes of the stones well, the periodic angle set (PWI) yielded lumpy artifacts, as indicated by the yellow arrows in Fig. 10(b). These lumpy artifacts were caused by the strong artifacts seen in the *xy*-plane images in Fig. 9 (marked by yellow boxes); these artifacts in US images were falsely detected as the surface of the stone when the brightness of the artifact was higher than the threshold for surface detection. The appearances of the stones in the rendered images (Fig. 10(b)) change with the threshold for surface detection. However, the APWI-C and APWI-S always yield the better shape of the stone than the PWI no matter what threshold was used. We will discuss this further by changing the threshold for detecting the surface in section IV.C.

D. In Vivo Carotid Artery

The effectiveness of the proposed angle sets was also observed with a human carotid artery. Fig. 11 shows the *xz*- and *yz*-planes of 3-D US images of an *in vivo* carotid artery when the periodic and two aperiodic angle sets were employed (N=49). The dynamic range was 45 dB. A multimedia movie is available showing all the cross-sections of the 3-D images (MM4). As the white arrows in Fig. 11 and MM4 indicate, APWI-C and APWI-S reduce the clutter artifacts inside the carotid artery compared to the PWI.

The contrast measured from volumetric artery and tissue regions (MM3) was 12.0 dB, 12.3 dB, and 12.3 dB. The contrast gains (0.3 dB) were much lower than those of the phantom results. These small enhancements might be due to the smaller number of PWs and freehand and physiological motion. This will be discussed in section IV.D. However, at some cross-sections, the grating lobe artifacts in the PWI were fairly reduced in the APWI-C and APWI-S; for example, at the *xz*-plane cross-section shown in the top panels of Fig. 11 (y = −3.37 mm), the contrast enhancement was 0.7 dB and 0.9 dB with APWI-C and APWI-S, respectively.

IV. Discussion

A. Experimental Verification of Simulation study

In this experiment, to verify the simulation study, 3D images (Fig. 4), lateral profiles (Fig. 5), and MSR enhancements (Fig. 6) were observed. The APWI methods reduced the artifact without compromising the spatial resolution and the frame rate in both the simulation and in the experiment. The artifacts around wires of APWI-C and APWI-S were less than those of PWI. The thickness of the wire that represents the spatial resolution at each depth was nearly the same over the three methods (PWI, APWI-C, and APWI-S).

The axial lobe artifacts below the wire were observed in the images at z = 10 mm for both the experimental and simulated results (top row of Fig. 4). These artifacts are usually observed near the transducer when the pitch between the transducer elements is larger than half wavelength [39]; the element pitch of the matrix array transducer used was 1.52λ, where λ is the wavelength. Although the axial lobe artifact can be reduced by using a transducer with a pitch of λ/2 [39], decreasing the pitch of a matrix array transducer costs more than a linear array transducer; a λ/2-matrix array would require 9 times more elements

than a 1.52λ -matrix array (i.e., 9,216 elements) if the aperture size should be maintained. The axial lobe artifact is caused not only by the pitch of transducer (grating lobe in the beam pattern of each PW) but also by the distribution of PW angles (grating lobe and sidelobe in the synthesized beam pattern of compounded PWs). Consequently, the axial lobe artifacts were reduced by using APWI-C and APWI-S.

When the mainlobe to axial lobe ratio (MAR) was measured using (4) with μ_{axial} instead of μ_{side}, the enhancement in MAR at the depth of 10 mm was 3.6 dB and 5.4 dB for experiment and 5.8 dB and 7.9 dB for simulation, when using APWI-C and APWI-S, respectively. These MAR enhancements were similar to MSR enhancements at 10 mm. However, for other depths, the enhancement in MAR was marginal (~0.8 dB) because the axial lobe artifact usually appears at the near field as shown in Fig. 4. Therefore, not only grating/sidelobe reduction but also the axial lobe reduction might have contributed to the contrast improvement at near field (< 20 mm).

In Fig. 5, the sidelobe level difference between the PWI and APWI methods at a depth of 10 mm was not as considerable as the difference at a depth of 20 mm. However, the MSR enhancements of APWI methods against PWI at 10 mm were as high as those at 20 mm in Fig. 6. This is because the MSR in Fig. 6 was measured by using the mean sidelobe level within volumes containing the whole sidelobe artifacts, as in Fig. S1, whereas the lateral profile Fig. 5 presents only 1-D information. In addition, the *yz*-plane cross-sectional images (Fig. S2) also corroborate the artifact reduction of APWI methods at a depth of 10 mm.

The performance (e.g., artifact reduction level) of the two APWI methods compared to the PWI depends on the imaging point location because a subset of transmitted PWs used for reconstruction varies with the imaging point. As described in section II.D, each imaging pixel was beamformed by compounding a subset of PWs, $\mathbb{S}(\mathbf{x})(\mathbb{S}(\mathbf{x}) \subset \mathbb{T}$ where $\mathbb{T}$ is a set of transmitted PWs), which reached out to the imaging point **x**. It is also elaborated in [31] with Figs. 7 and 8; despite the same number of transmitted PWs (N), the number of PWs compounded for a certain pixel (i.e., the number of PWs in $\mathbb{S}(\mathbf{x})$) could be different for each angle pattern. In addition, the arrangement of PW angles of each subset affects the beam pattern and artifacts at the certain imaging pixel. It is difficult to generalize the characteristics of all subsets because each subset will be a portion of the whole pattern, which will be different from each other. Although a portion of aperiodic set is still aperiodic, some subsets might not be as effective as others to suppress sidelobe levels. Different MSR enhancements across depths in Fig. 6 might have been caused by different subsets. It is interesting that both simulation and experimental results showed a lower MSR enhancement at 30 mm than at other depths. In addition, both results presented slightly better enhancement by APWI-S than by APWI-C in Fig. 6.

In Fig. 4, the dynamic range of 3D images was chosen to show well the difference in sidelobe artifacts between the three PWI and APWI methods and to obtain similar images between the experiment and simulation. The dynamic range of 3D images used for the experiment was smaller (35 dB) than that for the simulation (38 dB) because the experimental data had a lower signal-to-noise ratio (SNR) and stronger artifacts for all methods. In addition, the thickness of the wire in the experimental results was larger than

that in the simulation results because the wire used in the experiment had a thickness of approximately 0.3 mm, while the numerical wire in the simulation was composed of a series of point targets and did not have a thickness.

In this paper, we did not distinguish the artifacts from the sidelobes and grating lobes because the two types of artifacts spatially overlapped and were difficult to separate in the experimental images. In the simulation results, however, the grating lobe artifacts were more easily recognized than in the experimental results. Theoretically, the grating lobes, caused by the periodic PW angles of PWI, arise 2.7 mm apart from the mainlobe ($=\lambda/d_a$) [31], and they can be seen in Fig. 5 and Fig. S2. Although the grating lobe artifacts in the experiment were not as prominent as those in the simulation, it was interesting that the reduction in the mean sidelobe level (i.e., MSR enhancement) at each depth was similar between the simulation and experiment.

B. Quality-Assurance Phantom

The elevation resolutions in Table III are slightly better than the lateral resolutions because the size of the transducer (aperture size) in the y direction is larger than that in the x direction.

We used a cystic part of the phantom to quantitatively measure the contrast of the image. Since artifacts in the hypoechoic region are undesirable for many diagnostic ultrasound applications such as gallbladder imaging or carotid artery imaging, APWI can be beneficial to reduce such artifacts. Although we evaluated APWI using only a hypoechoic target, further investigation using different grayscale targets would be helpful for evaluating the method in terms of detection of a target with a small echo difference.

C. Gallbladder-Mimicking Phantom

In Fig. 9 and Fig. 10, aperiodic angles disperse the grating lobes in the beam pattern and mitigate the grating lobe-induced artifacts in the US images, consequently reducing the likelihood of false detection of hyperechoic materials. This result implies that the APWI methods would be helpful for characterizing the hyperechoic materials in a gall bladder or any other calcified stones in a black liquid pool in US images.

In Fig. 9, artifacts mainly appeared in the lateral (x) and elevational (y) directions. This cross pattern of artifacts was also observed in a previous study (Fig. 12 in [31]). This is related to the rectangular aperture of the matrix array transducer and is commonly shown in other studies where a rectangular aperture is used [10], [40]. In addition, although the APWI-S seems to have fewer artifacts than the APWI-C in the cross-section of Fig. 9, the opposite outcome can arise depending on which cross-section is observed. The overall image qualities of APWI-C and APWI-S were similar.

As shown in Fig. 10(b), APWI methods reconstructed stones with much more similar shapes to the real ones (Fig. 10(a)) than PWI images. Thresholds used for the surface detection of the stone were −25 dB and −32 dB for stone A and stone B, respectively. Even with different thresholds, the APWIs always showed better surface images than the PWI. Fig. S3 shows the 3-D rendered stones obtained from the PWI, APWI-C, and APWI-S images with

different thresholds. When the threshold is low (first row in Fig. S3), some strong artifacts are mistakenly detected as the stone surface. As the threshold increases, the size of the reconstructed stone shrinks. Even with different thresholds, the PWI suffers from the falsely detected area on the right-hand side of the stone due to the strong sidelobe artifacts in the 3-D US images (indicated by a yellow box in Fig. 9). In contrast, the APWI images showed fewer artifacts than the PWI for all thresholds, which makes it easier to find the optimal threshold value that yields the most similar images to the photos of the stones.

D. In Vivo Carotid Artery

Although they provided contrast enhancement (0.3 dB in volumetric measurement and 0.7 dB (APWI-C) and 0.9 dB (APWI-S) at one of the cross-sections), these gains were smaller than those of the phantom experiment and simulations. The first reason for the low improvement might be the low number of PW (N=49). Due to the limitation of the system, we divided the 1024-element array into four subarrays and repeated the TX/RX process 16 times with different pairs of subarrays to acquire a set of 1024-channel data with a 256-channel system. In the synthetic beampattern of APWI-C or APWI-S, the energy of the grating lobe is spread out to prevent the formation of a strong grating lobe-induced artifact by using its unique aperiodic angle pattern. However, the distinct feature of the aperiodic pattern becomes weaker as the number of PWs decreases, resulting in small contrast enhancements (as seen in Fig. 16 of [31]).

Another possible reason is the hand and physiological motion across the compounded images. Carotid artery images were obtained with free-hand scanning. In addition, the image acquisition rate was much lower due to the limitation of the number of channels of the ultrasound system. The acquisition time for a single volume was approximately 39.2 msec when the pulse repetition interval was 50 μsec and N=49. In addition, three data sets for the three different angle patterns were acquired sequentially, which means that the total data acquisition time was 117.6 msec. Although the data were obtained during diastole to minimize motion-induced artifacts, the vessel wall might have shifted approximately 0.3λ during the acquisition assuming that the velocity of the artery wall is 0.5 mm/s during diastole [41]. This physiological movement might have affected the quality of synthetic beamforming and the contrast enhancement of APWI.

E. Modification of Angle Pattern

In a previous study [31], the concentric ring pattern showed slightly higher resolution than expected because the effective radial range of angle was not considered. For a fairer evaluation across the imaging methods, we needed to control the spatial resolution of APWI-C more precisely because there is an apparent trade-off between the spatial resolution and the image contrast (or sidelobe level). In this paper, we suggested a modified version of the APWI-C for better control of the spatial resolution so that the spatial resolution can be a constant variable across the different imaging methods in the comparison study. As shown in Fig. 5 and 8, all three methods (PWI, APWI-C, and APWI-S) have the same spatial resolution, which allows for the decent comparison between the imaging methods in terms of the sidelobe level and the image contrast.

For further image quality enhancement, the angle pattern can be modified in different ways depending on applications and imaging probes. For example, the maximum steering angle can be lowered to compound more PWs at central region with a smaller PW angle interval for contrast sensitive applications, sacrificing the size of field-of-view and the spatial resolution. As another example, if the image quality of the central region is more important for diagnosis than that of the side region which is required only for anatomical localization, the PW seeds can be populated more densely around the origin in the $\alpha\beta$-plane instead of the uniform distribution. Numerous studies on the effective transducer element distribution [42]–[45] will be helpful for designing another version of the PW angle pattern optimized for a specific application because the transducer element distribution can be analogous to the PW angle distribution.

F. Comparison between APWI-C and APWI-S

We evaluated two types of aperiodic angle pattern: the concentric ring (APWI-C) and the sunflower (APWI-S). Both methods showed similar image quality improvement compared with the traditional PWI throughout all the simulations and experiments. Although the APWI-S showed better MSR in the wire simulation and experiment (Fig. 6), APWI-S was not always better than APWI-C. In the quality-assurance phantom experiment, APWI-C provided slightly higher contrast than APWI-S when $N = 149$ (Table II). However, these differences are too small to conclude which method is better than the other.

In addition, the effectiveness of one method over the other was easily reversed by changing the angle range, the number of PWs, or the image quality evaluation location. Therefore, we concluded that the two APWI methods provide similar performance in terms of spatial resolution and image contrast.

Comparing design rules, the concentric ring pattern is more complex than the sunflower pattern. Obtaining a concentric ring pattern requires the computation of many variables such as the number of rings, the radial interval between rings, and the seed angular interval of each ring (section II.A.2), whereas a sunflower pattern can be readily designed by two equations for α and β (section II.A.3). Hence, one may choose APWI-S for the simplicity of angle pattern design.

G. Limitation of the Experimental Setup

In this study, we used a small matrix array transducer with a size of 10 mm×10 mm. However, the transducer with a small aperture relative to the scanning volume is not beneficial for either PWI or APWI. Only approximately one-third of the transmitted PWs reached a depth of 20 mm on the center scanline in our experimental setup because the aperture was small and a PW propagated perpendicular to its wavefront with no divergence. In addition, the currently available matrix array transducers have a limited signal-to-noise ratio (SNR).

This small aperture and low SNR may have caused underestimation of the advantage from APWI. When the number of synthesized PWs at each depth decreases, the unique aperiodic angle pattern is less distinct, and the SNR further reduces. The advantage of APWI comes from its distinctive angle pattern, which reduces the grating lobe level in the beam pattern. In

this experiment, however, the number of PWs used for each depth was too small to exhibit its unique pattern, and the high noise level somewhat obscured the grating lobe artifacts.

A large pitch (1.52λ) of the transducer is another limiting factor. The maximum PW angle was set to 25° to obtain a sufficient field of view with a small matrix probe. However, this large steering angle with a large pitch could create a strong grating lobe when the PW is transmitted, and deteriorate the image quality. Image quality can be enhanced by reducing the maximum PW angle (i.e., smaller r_0 in Fig. 2) at the cost of a smaller field of view or by using a matrix array with a smaller pitch. The grating lobe artifact could also be reduced by lowering the imaging frequency to compensate for the large pitch at the expense of spatial resolution. As the fabrication technique evolves, a larger and more sensitive transducer will be available, and consequently, APWI will offer better contrast enhancement in 3-D US imaging.

The system with a lower number of channels than that of the array elements also limited our study. In the *in vivo* experiment, the number of TX/RX sequences was 49×16 to obtain a set of full-channel data with 49 PWs. Although such a low number of PWs is not favorable to prove the contrast enhancement of APWI, we could not increase the number of PWs due to the motion of the artery. To support full-channel acquisition, some research groups have developed 3D full-channel systems that manage up to 1024 channels [46]–[48]. If a full-channel system is available and the number of PWs increases, the contrast gain by APWI should be higher than what we found in this study. In addition, a sparse array can be used for achieving a shorter acquisition time with a limited-channel system by using various types of sparse arrays that have been proposed [17], [19], [49].

V. Conclusions

We experimentally evaluated the APWI-S and APWI-C in which the PW angles are distributed in an aperiodic manner to enhance the contrast of the 3-D US image without compromising the spatial resolution and the frame rate. We demonstrated our previous simulation study by a simulation-experiment comparison study. We proved the contrast enhancements of APWI-S and APWI-C compared with traditional PWI by phantom and *in vivo* experiments. In the quality-assurance phantom experiment, the APWI-C and APWI-S provided a CR approximately 2–3 dB higher than that of PWI without compromising the spatial resolution. In addition, in the gallbladder-mimicking phantom experiment, the APWI methods presented 3-D rendered stone images more similar to the real stones than the PWI. In the *in vivo* carotid artery image comparison, the APWI methods also provided better cross-sectional images with fewer clutter artifacts inside the artery than PWI. As the APWI reduces the energy of the grating lobe in the beam pattern and mitigates grating lobe/sidelobe-induced artifacts, it is beneficial for applications where a strong hyperechoic structure inside a hypoechoic region is examined or where clutter artifacts are critical. Although the image quality improvement of APWI methods was slightly underestimated due to the limitation of the experimental setup, all the results successfully showed the potential of APWI methods in terms of contrast enhancement.

Supplementary Material

Refer to Web version on PubMed Central for supplementary material.

Acknowledgments

This work was supported in part by the Korea Medical Device Development Grant funded by the Korea government (Ministry of Science and ICT, Ministry of Trade, Industry and Energy, Ministry of Health & Welfare, Ministry of Food and Drug Safety), Project Number: 9991007022, KMDF_PR_20200901_0009, (Tai-Kyong Song); and in part by Grants R01 CA239548 and R01HL148664 from National Institutes of Health (A Alizad and M Fatemi).

References

[1]. Fenster A, Parraga G, and Bax J, “Three-dimensional ultrasound scanning,” Interface Focus, vol. 1, no. 4, pp. 503–519, 2011. [PubMed: 22866228]

[2]. Provost J et al. , “3D ultrafast ultrasound imaging in vivo,” Phys. Med. Biol, vol. 59, no. 19, pp. L1–L13, 2014. [PubMed: 25207828]

[3]. Dave JK, Mc Donald ME, Mehrotra P, Kohut AR, Eisenbrey JR, and Forsberg F, “Recent technological advancements in cardiac ultrasound imaging,” Ultrasonics, vol. 84, pp. 329–340, 2017. [PubMed: 29223692]

[4]. Shattuck DP, Weinshenker MD, Smith SW, and von Ramm OT, “Explososcan: A parallel processing technique for high speed ultrasound imaging with linear phased arrays,” J. Acoust. Soc. Am, vol. 75, no. 4, pp. 1273–1282, 1984. [PubMed: 6725779]

[5]. von Ramm OT, Smith SW, and Pavy HG, “High-speed ultrasound volumetric imaging system. Part II. Parallel processing and image display,” IEEE Trans. Ultrason. Ferroelectr. Freq. Control, vol. 38, pp. 109–115, 1991. [PubMed: 18267564]

[6]. Hergum T, Bjastad T, Kristoffersen K, and Torp H, “Parallel beamforming using synthetic transmit beams,” IEEE Trans. Ultrason. Ferroelectr. Freq. Control, vol. 54, no. 2, pp. 271–279, 2007. [PubMed: 17328324]

[7]. Rabinovich A, Friedman Z, and Feuer A, “Multi-line acquisition with minimum variance beamforming in medical ultrasound imaging,” IEEE Trans. Ultrason. Ferroelectr. Freq. Control, vol. 60, no. 12, pp. 2521–2530, 2013. [PubMed: 24297018]

[8]. Tong L, Gao H, Choi HF, and D’hooge J, “Comparison of conventional parallel beamforming with plane wave and diverging wave imaging for cardiac applications: A simulation study,” IEEE Trans. Ultrason. Ferroelectr. Freq. Control, vol. 59, no. 8, pp. 1654–1663, 2012. [PubMed: 22899113]

[9]. Madore B, White PJ, Thomenius K, and Clement GT, “Accelerated focused ultrasound imaging,” Ultrason. Ferroelectr. Freq. Control. IEEE Trans, vol. 56, no. 12, pp. 2612–23, 2009.

[10]. Denarie B, Bjastad T, and Torp H, “Multi-line transmission in 3-D with reduced crosstalk artifacts: A proof of concept study,” IEEE Trans. Ultrason. Ferroelectr. Freq. Control, vol. 60, no. 8, pp. 1708–1718, 2013. [PubMed: 25004541]

[11]. Tong L, Ramalli A, Jasaityte R, Tortoli P, and D’Hooge J, “Multi-transmit beam forming for fast cardiac imaging-experimental validation and in vivo application,” IEEE Trans. Med. Imaging, vol. 33, no. 6, pp. 1205–1219, 2014. [PubMed: 24893253]

[12]. Ortega A et al. , “A comparison of the performance of different multiline transmit setups for fast volumetric cardiac ultrasound,” IEEE Trans. Ultrason. Ferroelectr. Freq. Control, vol. 63, no. 12, pp. 2082–2091, 2016. [PubMed: 27705857]

[13]. Lockwood GR, Talman JR, and Brunke SS, “Real-time 3-D ultrasound imaging using sparse synthetic aperture beamforming.,” IEEE Trans. Ultrason. Ferroelectr. Freq. Control, vol. 45, no. 4, pp. 980–8, 1998. [PubMed: 18244252]

[14]. Rasmussen M and Jensen J, “Comparison of 3-D synthetic aperture phased-array ultrasound imaging and parallel beamforming,” IEEE Trans. Ultrason. Ferroelectr. Freq. Control, vol. 61, no. 10, pp. 1638–1650, 2014. [PubMed: 25265174]

[15]. Yang M, Sampson R, Wei S, Wenisch TF, and Chakrabarti C, “High frame rate 3-D ultrasound imaging using separable beamforming,” J. Signal Process. Syst, vol. 78, pp. 73–84, 2015.

[16]. Flesch M et al. , “4D in-vivo ultrafast ultrasound imaging using a row-column addressed matrix and coherently-compounded orthogonal plane waves,” Phys. Med. Biol, vol. 62, p. aa63d9, 2017.

[17]. Roux E, Varray F, Lorena P, Cachard C, and Tortoli P, “Experimental 3-D Ultrasound Imaging with 2-D sparse arrays using focused and diverging waves,” Sci. Rep, vol. 8, pp. 1–12, 2018. [PubMed: 29311619]

[18]. Santos P, Haugen GU, Lovstakken L, Samset E, and D’Hooge J, “Diverging wave volumetric imaging using subaperture beamforming,” IEEE Trans. Ultrason. Ferroelectr. Freq. Control, vol. 63, no. 12, pp. 2114–2124, 2016. [PubMed: 27740479]

[19]. Bernal M, Cunitz B, Rohrbach D, and Daigle R, “High-frame-rate volume imaging using sparse-random-aperture compounding,” Phys. Med. Biol, vol. 65, no. 175002, pp. 1–13, 2020.

[20]. Holbek S et al. , “Ultrasonic 3-D vector flow method for quantitative in vivo peak velocity and flow rate estimation,” IEEE Trans. Ultrason. Ferroelectr. Freq. Control, vol. 64, no. 3, pp. 544–554, 2017. [PubMed: 27992335]

[21]. Correia M, Provost J, Tanter M, and Pernot M, “4D ultrafast ultrasound flow imaging: In vivo quantification of arterial volumetric flow rate in a single heartbeat,” Phys. Med. Biol, vol. 61, no. 23, pp. L48–L61, 2016. [PubMed: 27811406]

[22]. Voorneveld J et al. , “4-D echo-particle image velocimetry in a left ventricular phantom,” Ultrasound Med. Biol, vol. 46, no. 3, pp. 805–817, 2020. [PubMed: 31924419]

[23]. Gennisson J et al. , “4-D ultrafast shear-wave imaging,” IEEE Trans. Ultrason. Ferroelectr. Freq. Control, vol. 62, no. 6, pp. 1059–1065, 2015. [PubMed: 26067040]

[24]. Papadacci C, Finel V, Villemain O, Tanter M, and Pernot M, “4D ultrafast ultrasound imaging of naturally occurring shear waves in the human heart,” IEEE Trans. Med. Imaging, vol. 39, no. 12, pp. 4436–4444, 2020. [PubMed: 32857692]

[25]. Salles S et al. , “3D myocardial mechanical wave measurements: toward in vivo 3D myocardial elasticity mapping,” JACC Cardiovasc. Imaging, vol. 14, no. 8, pp. 1495–1505, 2021, doi: 10.1016/j.jcmg.2020.05.037. [PubMed: 32861651]

[26]. Papadacci C et al. , “Imaging the dynamics of cardiac fiber orientation in vivo using 3D Ultrasound Backscatter Tensor Imaging,” Sci. Rep, vol. 7, no. 1, pp. 1–9, 2017. [PubMed: 28127051]

[27]. Denarie B et al. , “Coherent plane wave compounding for very high frame rate ultrasonography of rapidly moving targets,” IEEE Trans. Med. Imaging, vol. 32, no. 7, pp. 1265–1276, 2013. [PubMed: 23549887]

[28]. Bae S, Kim P, and Song T, “Ultrasonic sector imaging using plane wave synthetic focusing with a convex array transducer,” J. Acoust. Soc. Am, vol. 144, no. 5, pp. 2627–2644, 2018. [PubMed: 30522306]

[29]. Montaldo G, Tanter M, Bercoff J, Benech N, and Fink M, “Coherent plane-wave compounding for very high frame rate ultrasonography and transient elastography,” IEEE Trans. Ultrason. Ferroelectr. Freq. Control, vol. 56, no. 3, pp. 489–506, Mar. 2009. [PubMed: 19411209]

[30]. Bae S and Song T-K, “Methods for grating lobe suppression in ultrasound plane wave imaging,” Appl. Sci, vol. 8, no. 10, pp. 1–8, Oct. 2018.

[31]. Bae S, Park J, and Song T, “Contrast and volume rate enhancement of 3D ultrasound imaging using aperiodic plane wave angles: a simulation study,” IEEE Trans. Ultrason. Ferroelectr. Freq. Control, vol. 66, no. 11, pp. 1731–1748, 2019. [PubMed: 31380753]

[32]. Chen K, Thomenius K, Khuri-Yakub BT, Lee H-S, and Sodini CG, “A column-row-parallel ultrasound imaging architecture for 3d planewave imaging and Tx 2nd-order harmonic distortion (HD2) reduction,” in IEEE International Ultrasonics Symposium, Sep. 2014, vol. 1, pp. 317–320.

[33]. Martínez O, Martín CJ, Godoy G, and Ullate LG, “2D array based on Fermat spiral for ultrasound imaging,” Ultrasonics, vol. 50, no. 2, pp. 280–289, 2010. [PubMed: 19819510]

[34]. Viganó MC, Toso G, Caille G, Mangenot C, and Lager IE, “Sunflower array antenna with adjustable density taper,” Int. J. Antennas Propag, vol. 2009, no. Article ID 624035, pp. 1–10, 2009.

[35]. Yoon H and Song TK, “Sparse rectangular and spiral array designs for 3D medical ultrasound imaging,” Sensors (Switzerland), vol. 20, no. 1, 2020.

[36]. Yu J, Yoon H, Khalifa YM, and Emelianov SY, “Design of a volumetric imaging sequence using a Vantage-256 ultrasound research platform multiplexed with a 1024-element fully sampled matrix array,” IEEE Trans. Ultrason. Ferroelectr. Freq. Control, vol. 67, no. 2, pp. 248–257, 2020. [PubMed: 31545718]

[37]. Zhao J, Wang Y, Yu J, Guo W, Li T, and Zheng YP, “Subarray coherence based postfilter for eigenspace based minimum variance beamformer in ultrasound plane-wave imaging,” Ultrasonics, vol. 65, pp. 23–33, 2016. [PubMed: 26582600]

[38]. Tempkin BB, Sonography scanning principles and protocols, 4th ed. St. Louis, 2015.

[39]. Jensen J, Stuart M, and Jensen J, “Optimized plane wave imaging for fast and high quality ultrasound imaging,” IEEE Trans. Ultrason. Ferroelectr. Freq. Control, vol. 63, no. 11, pp. 1922–1934, 2016. [PubMed: 27824568]

[40]. Yang M et al., “High volume rate, high resolution 3D plane wave imaging,” in IEEE International Ultrasonics Symposium, Sep. 2014, pp. 1253–1256.

[41]. Golemati S, Sassano A, Lever MJ, Bharath AA, Dhanjil S, and Nicolaides AN, “Carotid artery wall motion estimated from b-mode ultrasound using region tracking and block matching,” Ultrasound Med. Biol, vol. 29, no. 3, pp. 387–399, 2003. [PubMed: 12706190]

[42]. Ramalli A, Boni E, and Savoia AS, “Density-tapered spiral arrays for ultrasound 3-D imaging,” IEEE Trans. Ultrason. Ferroelectr. Freq. Control, vol. 62, no. 8, pp. 1580–1588, 2015. [PubMed: 26285181]

[43]. Schwartz JL and Steinberg BD, “Ultrasparse, ultrawideband arrays,” IEEE Trans. Ultrason. Ferroelectr. Freq. Control, vol. 45, no. 2, pp. 376–393, 1998 [PubMed: 18244190]

[44]. Haupt RL, “Thinned arrays using genetic algorithms,” IEEE Trans. Antennas Propag, vol. 42, no. 7, pp. 993–999, 1994.

[45]. Wang X, Yao M, Zhang F, and Dai D, “Synthesis of sparse concentric ring arrays based on fitness-associated differential evolution algorithm,” Int. J. Antennas Propag, vol. 2019, 2019..

[46]. Jensen JA et al. , “SARUS: A synthetic aperture real-time ultrasound system,” IEEE Trans. Ultrason. Ferroelectr. Freq. Control, vol. 60, no. 9, pp. 1838–1852, 2013. [PubMed: 24658717]

[47]. Petrusca L et al. , “Fast volumetric ultrasound B-mode and Doppler imaging with a new high-channels density platform for advanced 4D cardiac imaging/therapy,” Appl. Sci, vol. 8, no. 2, 2018.

[48]. Risser C et al. , “Real-time volumetric ultrasound research platform with 1024 parallel transmit and receive channels,” Appl. Sci, vol. 11, no. 13, 2021.

[49]. Ramalli A et al. , “High-frame-rate tri-plane echocardiography with spiral arrays: From simulation to real-time implementation,” IEEE Trans. Ultrason. Ferroelectr. Freq. Control, vol. 67, no. 1, pp. 57–69, 2020. [PubMed: 31514130]

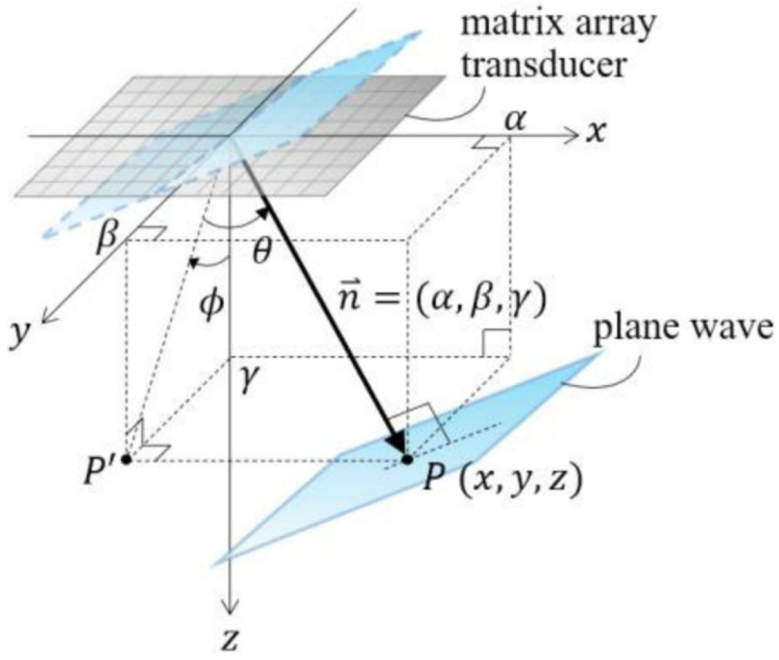

Fig. 1.

Definition of the propagation angle of a PW transmitted by a matrix array transducer. We express the propagation direction (or steering angle) of a PW with (α,β) because $\vec{n}$ is a normal vector of wavefront of PW and $\alpha^2 + \beta^2 + \gamma^2 = 1$. Point P' is the orthogonal projection of point P onto the yz plane and the angle θ and ϕ are the lateral and elevational angles of the PW.

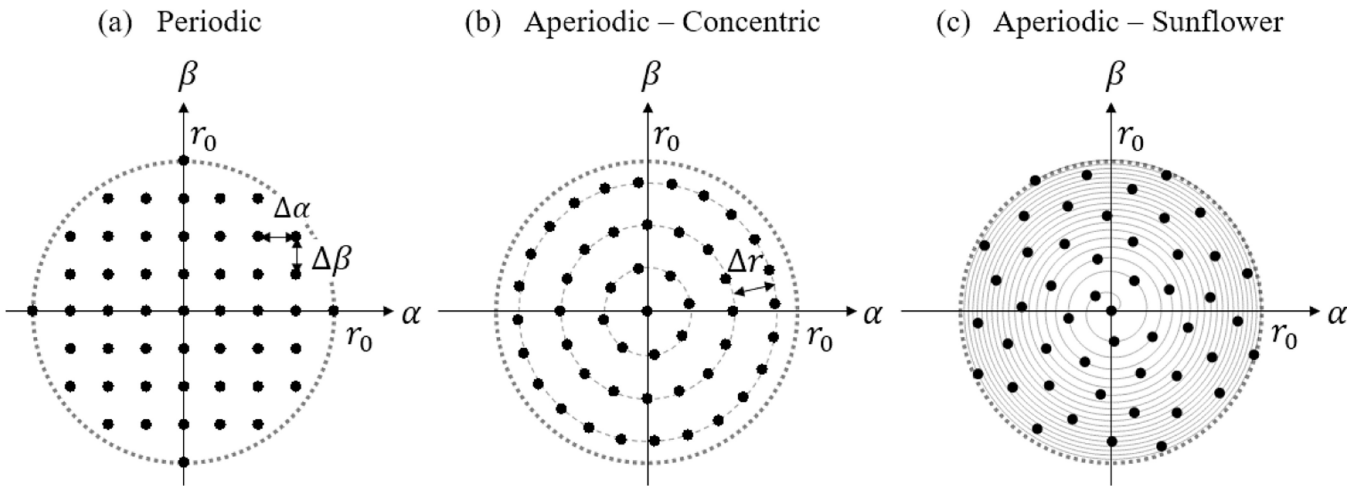

Fig. 2.

(a) Periodic PW angle patterns used for conventional PWI. (b), (c) Aperiodic concentric ring and sunflower PW angle patterns for APWI-C and APWI-S, respectively. Each black dot represents the steering angle of a PW transmitted by a 2-D matrix array transducer.

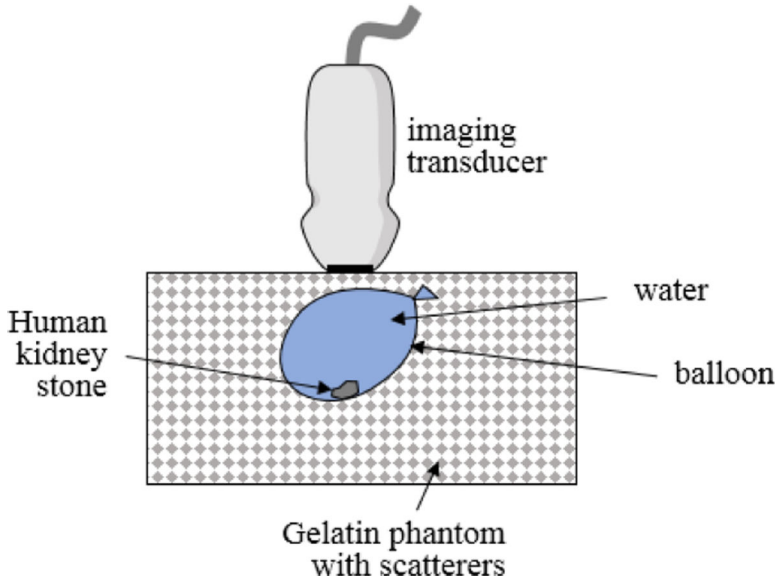

Fig. 3.

Gallbladder-mimicking phantom. A water-filled balloon and a human kidney stone were used for mimicking a gallbladder and a gallstone, respectively.

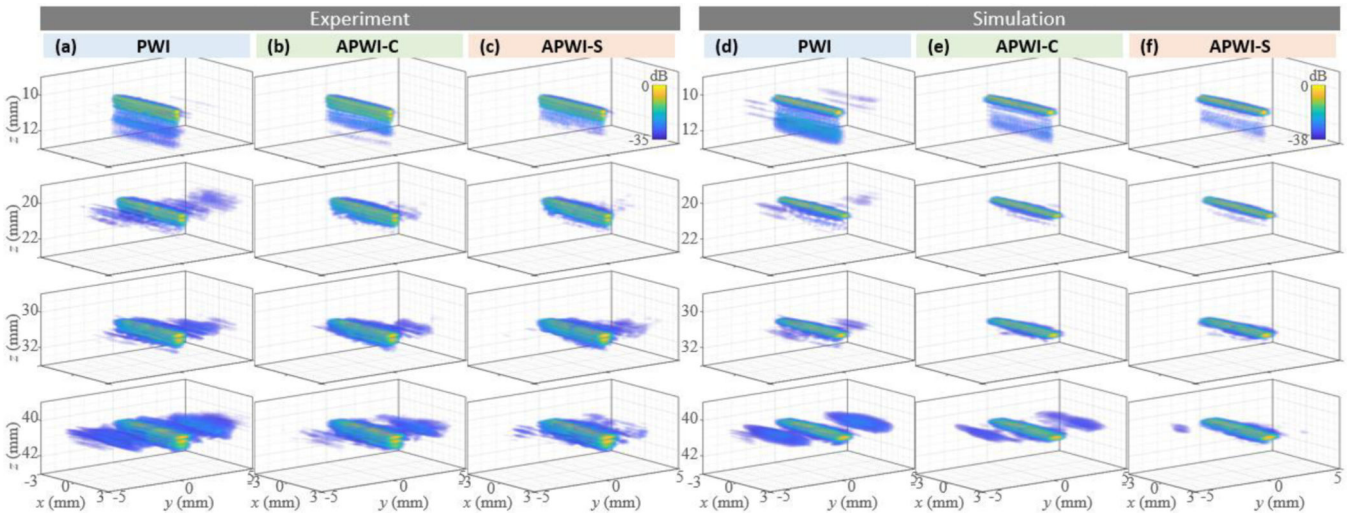

Fig. 4.

3-D US images of four wires in parallel with the *x*-axis at a depth (*z*) of 10, 20, 30, and 40 mm (from top to bottom) acquired from (a)–(c) experimental and (d)–(f) simulation results by using (a), (d) PWI, (b), (e) APWI-C, and (c), (f) APWI-S. The hyperechoic wires are shown in yellow, and the artifacts are shown in blue around the wires. The artifact reductions by APWI-C and APWI-S were observed in experimental results as well as in the simulation results.

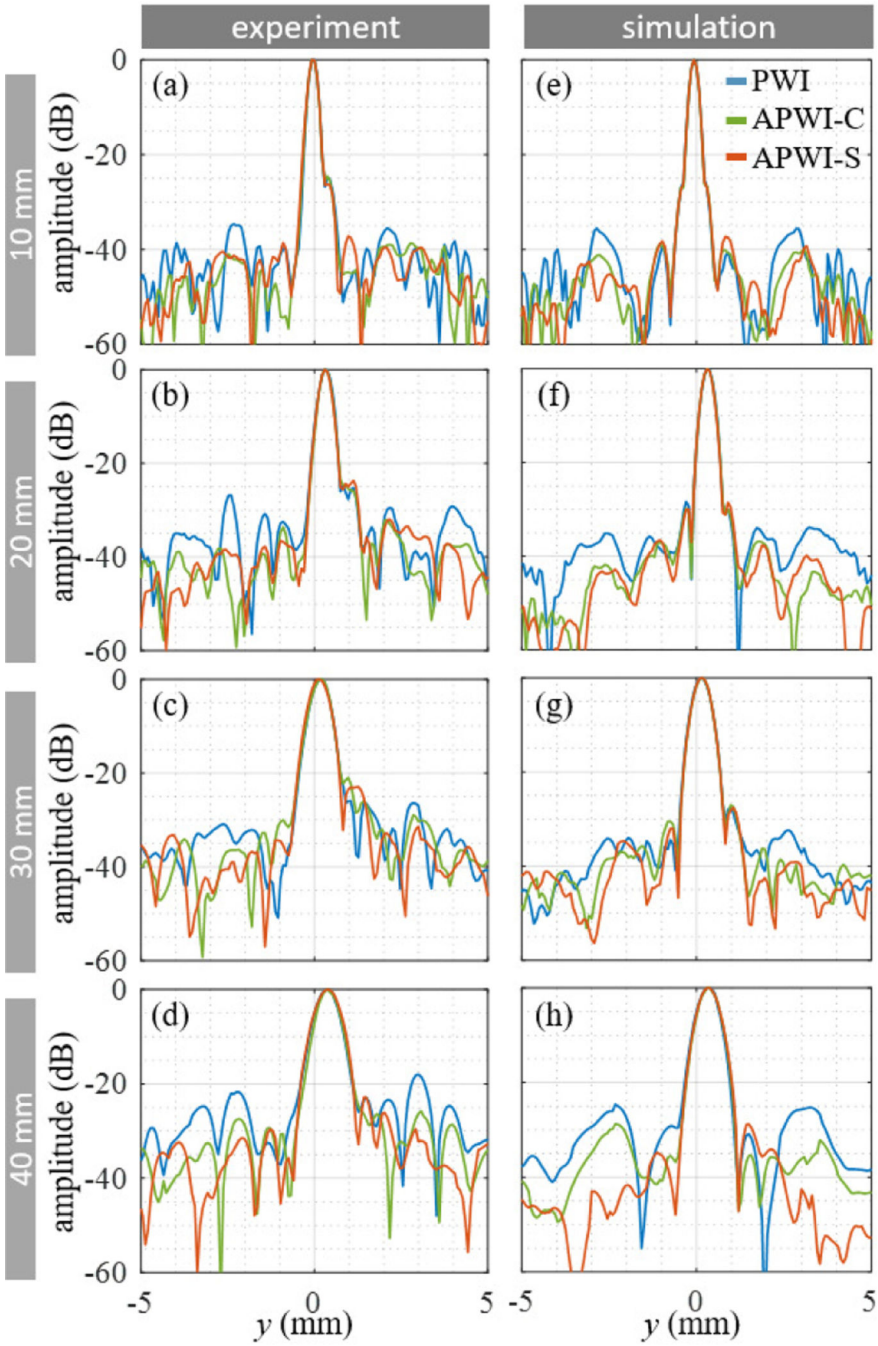

Fig. 5.

Profiles of wire targets along the y axis at the depth (z) of (a), (e) 10, (b), (f) 20, (c), (g) 30, and (d), (h) 40 mm at x = 0 mm, obtained from (a)–(d) experiment and (e)–(h) simulation, which show the beam width of the mainlobe and level of sidelobes at each imaging depth. Profiles were taken from the 3-D images of Fig. 4. As shown in the simulation results (e)–(h), the experimental results (a)–(d) also demonstrated that both APWI-C and APWI-S mitigate sidelobe artifacts without compromising the spatial resolution.

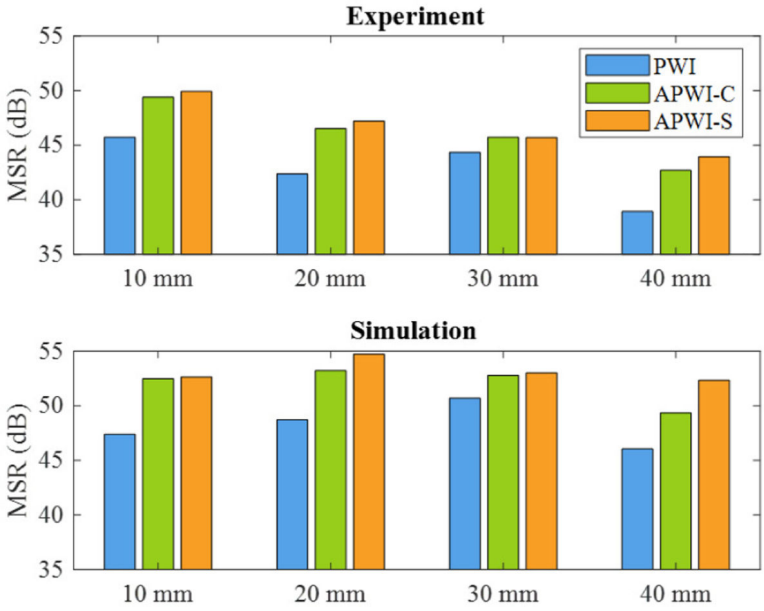

Fig. 6.

Mainlobe-to-sidelobe energy ratios (MSRs) of (a) the experiment and (b) the simulation 3-D images of four wires (shown in Fig. 4) reconstructed by using PWI and the proposed APWI-C and APWI-S at imaging depths (10, 20, 30, and 40 mm).

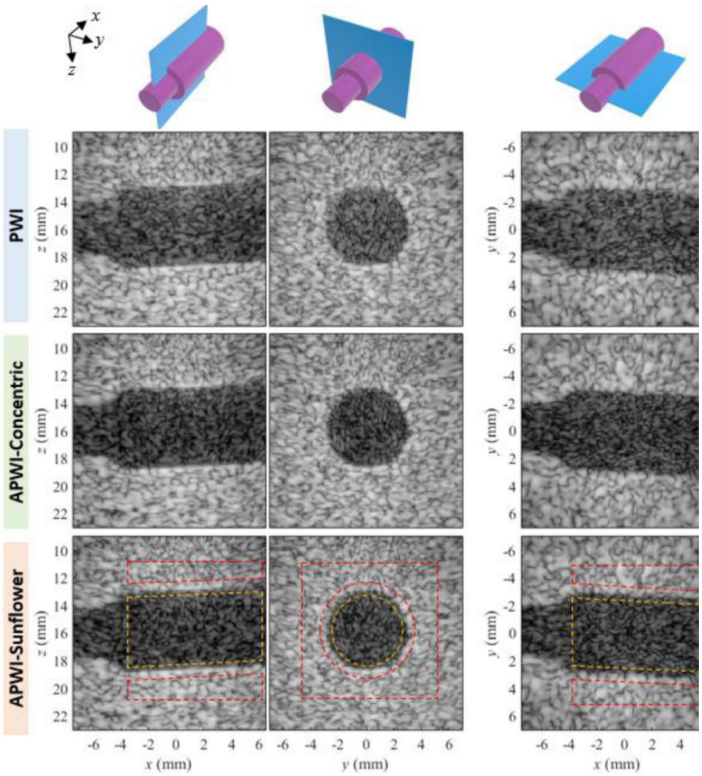

Fig. 7.

Cross-sections of 3-D US images of a cylindrical cyst in the commercial phantom in the *xz*-plane, *yz*-plane, and *xy*-plane (from left to right) reconstructed by using PWI, APWI-C, and APWI-S (from top to bottom) with a dynamic range of 50 dB. APWI methods provide better contrast resolution than conventional PWI. The number of PWs used was 81 for all methods (N=81). A multimedia movie is available for all the cross-sections of the volume (MM1). The dashed yellow and red boxes represent the cyst region and background region used for contrast measurement, respectively.

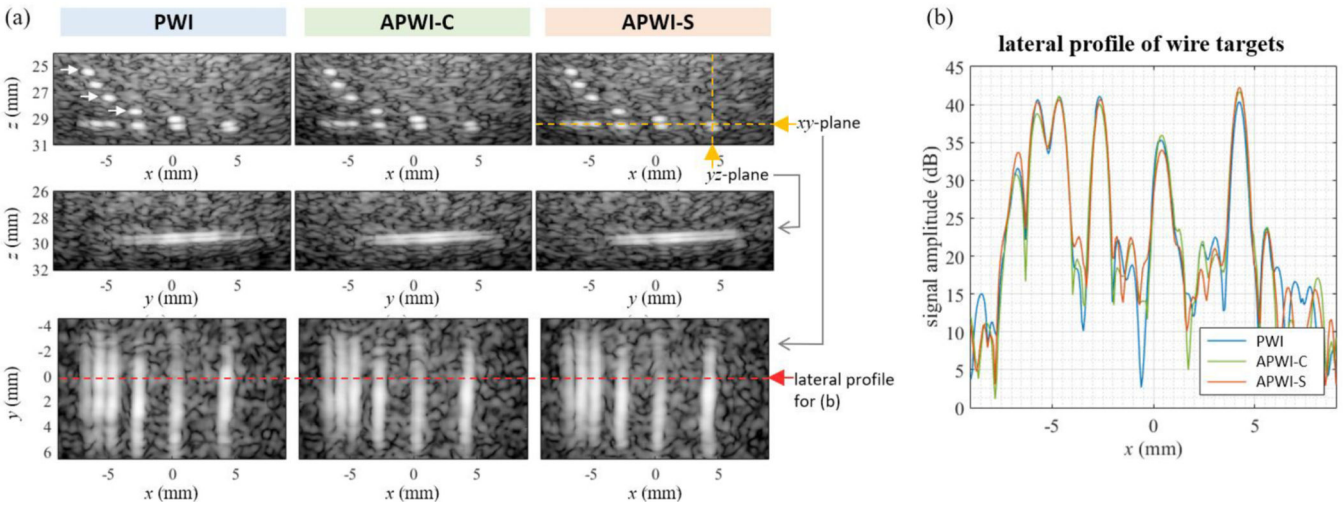

Fig. 8.

Cross-section US images of wire targets in the commercial phantom reconstructed by using the PWI (periodic angle set), APWI-C (concentric ring angle set), and APWI-S (sunflower angle set). (a) Cross-section images of the *xz* (*y* = 0), *yz* (*x* = 4.4 mm), and *xy* (*z* = 29.3 mm) planes (from top to bottom); the positions of the *yz* and *xy* cross-sections are indicated by yellow lines in the top-right panel of (a). (b) Lateral profiles at *y* = 0 mm and *z* = 29.3 mm; the position of the lateral profile is marked by a red line in the bottom-right panel of (a).

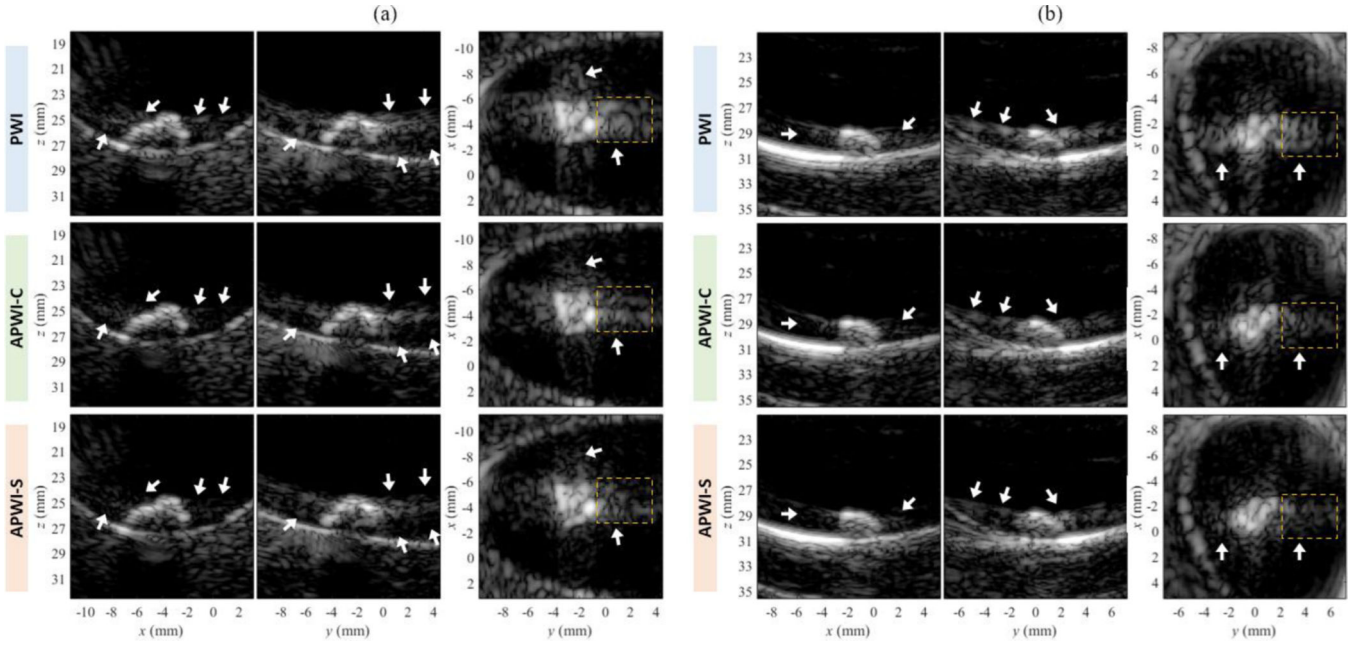

Fig. 9.

Cross-sections of the 3-D US images of the gallbladder-mimicking phantom ((a) stone A and (b) stone B). The images were reconstructed by using PWI, APWI-C, and APWI-S (from top to bottom). The hyperechoic stone is visible at the center of images. The APWI methods provide images with less artifacts around the stones compared to the PWI (white arrows and yellow boxes). The yellow box indicates the artifacts spread out in the $+y$ direction, which caused the false detection of stone surface in the 3-D rendered image of PWI (indicated by yellow arrows in the left panels in Fig. 10(b)). The dynamic range of the images is 50 dB.

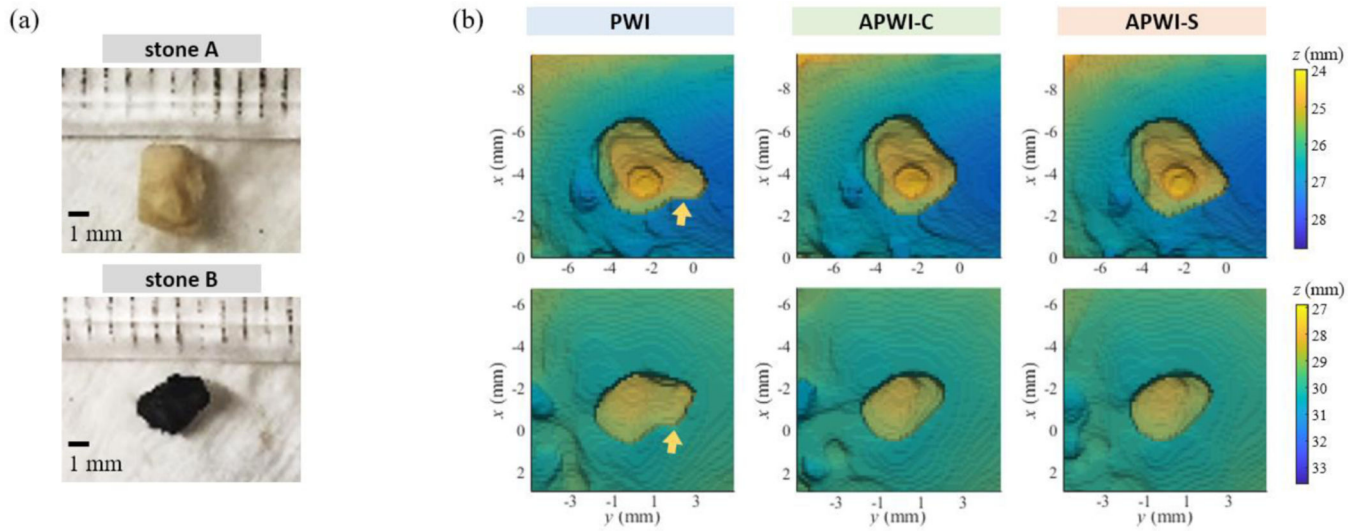

Fig. 10.

(a) Top views of the stones in the gallbladder-mimicking phantom. (b) Surface images of stone A (top row) and stone B (bottom row) reconstructed from the 3-D US images obtained using the PWI, APWI-C, and APWI-S. The depth of the surface was color-coded.

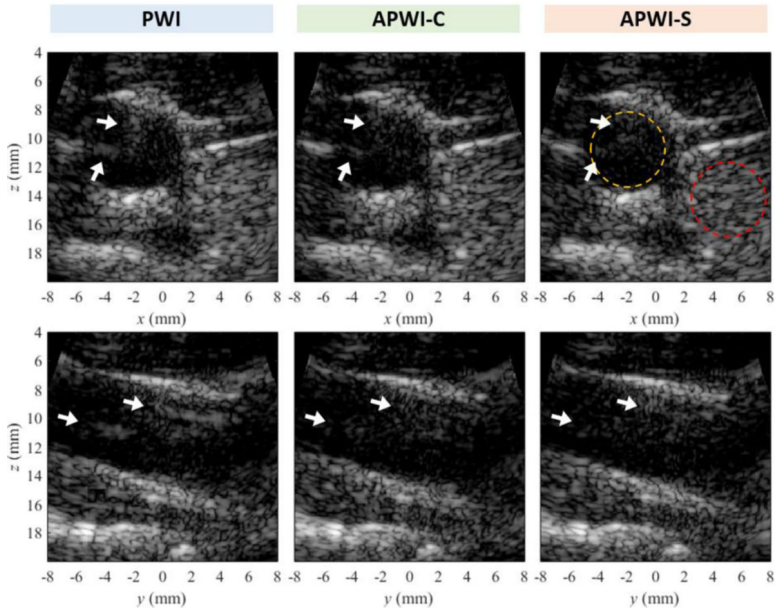

Fig. 11.

In vivo carotid artery images in the transverse view (top panels, $y = -3.37$ mm) and in the longitudinal view (bottom panels, $x = -3.67$ mm) obtained using PWI (left), APWI-C (center) and APWI-S (right). The two proposed PW sets (APWI-C and APWI-S) suppressed the artifacts inside the carotid artery (white arrows). A multimedia movie for all cross-sections of the 3-D images is available (MM4). The dynamic range is 45 dB. The dashed yellow and red boxes represent the vessel region and background tissue region used for contrast measurement, respectively.

Table I.

Parameters used for experiments

Number of transducer elements	32×32
Transducer pitch	0.3 mm
Transmit center frequency	7.8 MHz
Number of cycles	1
Maximum steering angle of PW	25°
Number of PWs (N)	49, 81, 113, or 149
Apodization window	Tukey window (25%)

Table II.

CR and CNR measured from the 3-D cylindrical cyst phantom images (Fig. 7). The 3-D region of cyst and background used for the contrast measurement is shown in MM2. The 3-D cyst image (N=81) is shown in Fig. 7 and MM1.

N	Method	CR (dB)	CNR
81	PWI	13.5	1.82
	APWI-C	16.3	2.27
	APWI-S	16.3	2.26
113	PWI	15.0	2.05
	APWI-C	17.1	2.37
	APWI-S	17.4	2.41
149	PWI	16.1	2.19
	APWI-C	18.0	2.50
	APWI-S	17.9	2.47

Table III.

LATERAL AND ELEVATIONAL RESOLUTIONS MEASURED FROM THE THREE TARGETS IN THE WIRE PHANTOM IMAGES, WHICH SHOWS THAT THE SPATIAL RESOLUTION OF ALL THE METHODS ARE EQUIVALENT. THE THREE TARGETS ARE INDICATED BY WHITE ARROWS AT THE TOP-LEFT PANEL IN FIG. 8.

N	Method	Lateral Resolution (mm)			Elevational Resolution (mm)		
		target 1	target 2	target 3	target 1	target 2	target 3
81	PWI	0.72	0.72	0.71	0.66	0.69	0.65
	APWI-C	0.7	0.7	0.71	0.63	0.69	0.65
	APWI-S	0.69	0.69	0.69	0.62	0.68	0.69
113	PWI	0.75	0.75	0.65	0.65	0.71	0.72
	APWI-C	0.74	0.74	0.65	0.64	0.67	0.68
	AWPI-S	0.73	0.68	0.66	0.64	0.65	0.66